ACS NANO

www.acsnano.org

ARTICLE

Correlative Fluorescence and Transmission Electron Microscopy Assisted by 3D Machine Learning Reveals Thin Nanodiamonds Fluoresce Brighter

Haotian Wen, David Kordahl, Inga C. Kuschnerus, Philipp Reineck, Alexander Macmillan, Huan-Cheng Chang, Christian Dwyer, and Shery L. Y. Chang*

Cite This: *ACS Nano* 2023, 17, 16491−16500

Read Online

ACCESS | Metrics & More | Article Recommendations | Supporting Information

ABSTRACT: Nitrogen vacancy (NV) centers in fluorescent nanodiamonds (FNDs) draw widespread attention as quantum sensors due to their room-temperature luminescence, exceptional photo- and chemical stability, and biocompatibility. For bioscience applications, NV centers in FNDs offer high-spatial-resolution capabilities that are unparalleled by other solid-state nanoparticle emitters. On the other hand, pursuits to further improve the optical properties of FNDs have reached a bottleneck, with intense debate in the literature over which of the many factors are most pertinent. Here, we describe how substantial progress can be achieved using a correlative transmission electron microscopy and photoluminescence (TEMPL) method that we have developed. TEMPL enables a precise correlative analysis of the fluorescence brightness, size, and shape of individual FND particles. Augmented with machine learning, TEMPL can be used to analyze a large, statistically meaningful number of particles. Our results reveal that FND fluorescence is strongly dependent on particle shape, specifically, that thin, flake-shaped particles are up to several times brighter and that fluorescence increases with decreasing particle sphericity. Our theoretical analysis shows that these observations are attributable to the constructive interference of light waves within the FNDs. Our findings have significant implications for state-of-the-art sensing applications, and they offer potential avenues for improving the sensitivity and resolution of quantum sensing devices.

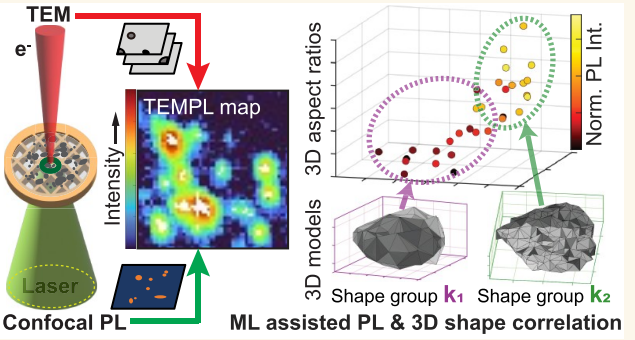

KEYWORDS: *fluorescent nanodiamond, nitrogen vacancy centers, machine learning, transmission electron microscopy, photoluminescence, electron energy loss spectroscopy*

INTRODUCTION

Atom-like solid-state quantum emitters have excellent potential as nanosensors, offering high spatial resolution and minimized disturbance to the host. Among the quantum emitters available, nitrogen vacancy (NV) centers in fluorescent nanodiamonds (FNDs) have attracted immense interest owing to their room-temperature operation, exceptionally high photo- and chemical stability, and excellent biocompatibility.[1−4] Such advantages have seen FNDs utilized as sensors of local temperature,[5,6] electric[7] and magnetic fields,[8−10] local crystallographic strain,[11] and single molecules.[12] Recently, detection of HIV with a sensitivity 5 orders of magnitude better than conventional gold nanoparticles[13] has further demonstrated the potential of FNDs as highly competitive biosensors for medical diagnostics.

Most FND-based sensors rely on optical emission, and thus, their sensitivity improves with increasing photoluminescence (PL) brightness. Hence, various routes to improved brightness have been pursued, such as by increasing NV concentration,[14,15] FND surface modification,[16−20] and tuning of

Received: January 29, 2023
Accepted: August 14, 2023
Published: August 18, 2023

https://doi.org/10.1021/acsnano.3c00857
ACS Nano 2023, 17, 16491−16500

the annealing process.[21,22] In addition, the size and shape of the FND particles are vital parameters. Generally, the closer the NVs are to the analyte, the better the sensitivity. Hence, there is a strong push to create ever smaller FNDs (≤20 nm) in which all NVs are necessarily close to the FND surface. However, achieving an adequate number of NVs to give high, stable fluorescence in such small FNDs has proven very challenging.[23] In this context, particle shape can be crucial: A particle that is, for example, 100 nm in two dimensions and 20 nm in the third dimension could potentially achieve both high fluorescence and high NV surface proximity.

On the other hand, understanding which of the many possible factors are important to the brightness of NVs (and other color centers) in FNDs is extremely challenging. Thus, there has been intense debate in the literature regarding the pertinent factors, including the particle size and shape. For example, measurements from FND ensembles show that the PL intensity generally decreases with decreasing particle size.[24,25] Since most FND fabrication is a top-down process, whereby larger diamond crystals (μm sized) are milled to smaller sizes,[24,26] the resultant FNDs typically comprise a broad distribution of sizes and shapes. This lack of uniformity has inspired single-particle level studies, using correlative scanning electron microscopy (SEM) and atomic force microscopy (AFM),[27,28] which have concluded that, depending on the fabrication process and the nominal particle size, there is no correlation, or at best moderate correlation, between the PL intensities and particle sizes. Moreover, numerous studies have shown that even individual FND particles of the same size and same fabrication process can exhibit a 4−5-fold variation in brightness.[27,29] Such variations are highly problematic for potential scale-ups of nanosensor applications: For FND scanning probes as near-field sensors, it can make the selection of an "ideal" FND particle a laborious process;[30] for accurately positioned nanosensors, such variations can result in substantial, undesired variability between different locations.[31] On the other hand, studies of shape effects are scarce, with only a few recent works reporting that FND particles can have high aspect ratios.[3,32] No correlations between the particle shape and PL brightness have been reported.

To date, measurements of FND brightness have been performed either on large ensembles of particles or on a small number of individual particles.[3,24,33] Ensemble measurements offer rapidity and broad representability, but run the risk of missing factors associated with individual particles, such as the influence of size and shape on the electromagnetic environments of color centers.[34] This has motivated studies on individual particles using confocal PL combined with SEM or AFM.[27,28,35−37] Unfortunately, while the latter studies have provided more information, it can be argued that they are inconclusive and contradictory regarding the dependence of PL brightness on particle size and shape. This could be attributable to the limited spatial resolution of SEM and AFM, and the lack of thickness information in the case of SEM, which often cannot resolve detailed structural features to provide accurate measurements of particle shapes.

To overcome these challenges, here, we have developed a method based on correlative transmission electron microscopy and photoluminescence (TEMPL). TEMPL allows a direct correlation of the fluorescence brightness and (quasi)-3D size and shape of individual FND nanoparticles. PL provides optical information with exquisite energy resolution, and TEM provides structural information with exquisite spatial resolution. Unsupervised machine learning (ML), using generalized 3D shape descriptors, is used to analyze correlations between the PL brightness and the 3D shape of FND particles. The automation provided by machine learning allows TEMPL to be applied to large sample areas (2−3 orders of magnitude larger than a typical TEM field of view) containing a statistically significant number of particles.

Using our machine-learning-assisted TEMPL method and supplemented by our theoretical analysis, we demonstrate that the FND particle shape, combined with the presence of suitable thin substrate or surrounding medium, can produce a substantial increase in the PL brightness. In particular, we show that a thin, flake-shaped FND particle morphology, irrespective of the particle diameter, can host NV centers that exhibit up to several times greater brightness than thicker particles. Further substantiated by our theoretical calculations, our results demonstrate that a thin particle morphology could provide a possible approach to brighter FNDs containing near-surface NVs, thereby advancing the sensitivity and resolution of FND-based quantum sensors.

The layout of this article is as follows. In the first half, we describe the machine-learning-assisted TEMPL method that we have developed. We describe our methods to correlate data from TEM and PL experiments, our procedure for retrieving 3D shapes of individual FND particles, and our machine-learning-based shape analysis algorithm. In the second half, we describe results obtained from an application of TEMPL to the 3D morphology−structure−photoluminescence relationships of FND, as well as a theoretical analysis of the Purcell effect in FND. In the final sections, we present a conclusion and additional details on materials and methods.

RESULTS/DISCUSSION

Machine-Learning-Assisted TEMPL. *Correlative TEM and PL.* Figure 1 illustrates the TEMPL method. To achieve an accurate correlation of TEM and PL data, it is essential to use a sample substrate that works for both measurements with appropriate markers for registration. For this purpose, we use a TEM grid featuring square windows with a 10 nm uniformly thick *a*-Si_3N_4 substrate, which provides low background

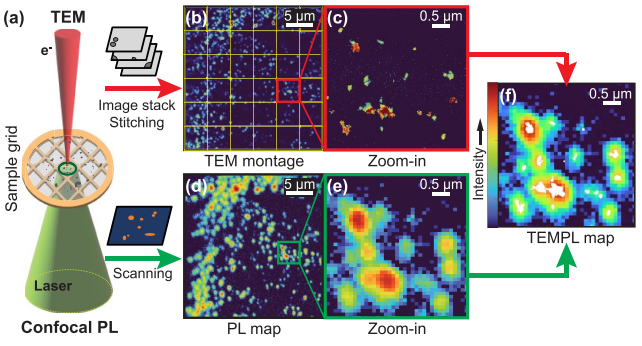

Figure 1. Correlative TEMPL. (a) BF-TEM montage imaging and confocal PL mapping are applied to the same sample region; (b, c) BF-TEM montage exhibiting local particle distribution and their nanostructures and zoom-in of an arbitrary subarea; (d, e) Corresponding confocal PL map and zoom-in; (f) TEMPL map of the subarea exhibiting precise one-to-one correlation between PL (multicolored) and BF-TEM (white). In (f), the variation of BF-TEM intensity is omitted for visualization.

https://doi.org/10.1021/acsnano.3c00857
ACS Nano 2023, 17, 16491−16500

contrast in TEM imaging and minimal background fluorescence in PL. Moreover, as will be explained later, such a substrate closely mimics the electromagnetic environment that FND particles would experience in free space.

TEM has a field of view that is typically 3 orders of magnitude smaller than that of PL. To overcome this, a large number (thousands) of TEM images are acquired to effectively match the fields of view (Figure 1(a)). Bright-field (BF) TEM imaging is used here for its rapidity. Moreover, in the case of a weakly scattering sample, such as FND, the BF intensity varies approximately linearly with sample thickness for particles oriented away from major zone axes (as validated below), enabling a relatively simple quantification of the local thickness within individual FND particles. The latter information enables us to obtain quasi-3D particle shapes that are used to correlate with the PL intensities.

One of the most challenging aspects of the TEMPL method is to achieve an accurate registration between the PL and TEM data sets. Our registration procedure can be divided into three main steps. First, the TEM images are "stitched" together using cross-correlation of overlapping edge regions to construct a TEM montage map which covers the same fields of view as the PL map (Figure 1(b,d)) (details in the SI). Second, the TEM montage and the PL map are coarsely registered, using the edges of patterned window, and with the application of an affine transformation to correct the scaling, rotation, skew distortion, and translation (Figure S2). Third, a final affine transformation is applied to align the particle positions obtained from the higher resolution TEM images with the centroids of peaks in the PL map (Figure 1(f) and SI).

In this demonstration of the TEMPL method, we have taken care to ensure that the measured PL brightnesses of individual particles come from well-isolated particles. This cautious approach was taken to ensure that the relatively poor spatial resolution of the PL signal did not compromise our results. A disadvantage of this approach is that only a fraction of the particles (20% in the FND analysis described later) are ultimately included. In addition, we can use the higher spatial resolution information in the TEM images to retrieve a superresolved PL signal with the *a priori* knowledge of the PL point-spread function.

Retrieval of Quasi-3D Particle Shapes. Although electron tomography is arguably the most established technique for reconstructing the 3D shapes of nanoparticles, standard implementations require a tilt series containing more than 100 members, which is impractical in the context of TEMPL, where 1000 images are already necessary to cover the large field of view. Tomographic reconstructions also suffer from the "missing wedge" problem, which leads to artificial shape elongation.[38−40] Instead, we opted for a simpler approach to retrieve the quasi-3D shape information from the local sample thickness. The approach assumes that the 2D projection plane of the sample is a mirror plane (see SI Section IV for further details). This assumption is common in the field of computer vision[41,42] and has also been used in the context of atomic-resolution electron tomography.[43,44] Although some 3D information is inevitably lost, the retrieved quasi-3D information proves to be sufficient for our categorization and analysis. Moreover, the approach is rapid and requires minimal imaging data and is thus suited to the large field of view mandated by TEMPL.

To obtain the local sample thickness, we used the fact that the BF-TEM image intensity varies linearly with thickness for homogeneous, weakly scattering samples oriented away from major zone axes. To verify the latter statement, we have tested it against both AFM and annular dark-field scanning transmission electron microscopy (ADF-STEM), the latter two being established techniques for determination of local sample thickness.[45−48] The comparison is shown in Figure 2(a,b). Agreement to within 6% is obtained over a broad range

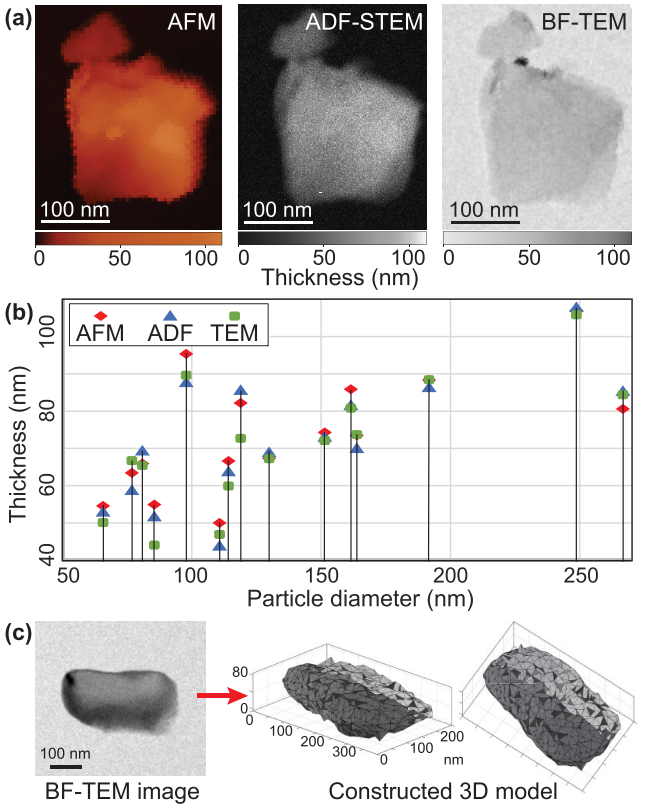

Figure 2. Verification of BF-TEM for local thickness and quasi-3D shape retrieval. (a) AFM, ADF-STEM, and BF-TEM imaging of the same exemplar FND particle, with the color (or gray scale) bar indicating the local thickness for each image. (b) Comparison of measured thicknesses of 18 exemplar FND particles spanning a broad range of sizes and shapes. (c) Exemplar retrieval of quasi-3D particle shape from its BF-TEM image.

of particle sizes and shapes, which is an acceptable error. Although it would be possible to do so, here we choose not to use AFM or ADF-STEM directly in the TEMPL method, as their acquisition times are an order of magnitude slower than BF-TEM.

Machine Learning-Based Shape Analysis. To enable a statistical analysis of the PL brightness and 3D shape distribution of the FND particles, we have developed an unsupervised machine learning approach that utilizes a clustering method (for details see SI Section VI). Such unsupervised methods do not require training data and are therefore not prone to biases that may exist in training data. Our ML approach employs the first three 3D Hu moments H_1^{3D},H_2^{3D}, andH_3^{3D} as the shape descriptors. The 3D Hu moments differ from the 2D Hu moments[49] often employed in the field of computer vision, as well as electron microscopy.[50,51] The main advantage of (both 2D and 3D) Hu moments is that they provide shape parametrization that is independent of the size, spatial location, and orientation of the

https://doi.org/10.1021/acsnano.3c00857
ACS Nano 2023, 17, 16491−16500

particle. They can also be computed efficiently, which is important for the throughput of the TEMPL method. Here we have employed only the first three 3D Hu moments; however, we find that this number permits sufficiently accurate analysis of the FND shapes (see SI Section V and Figure S3 for further details).

The first three 3D Hu moments can be defined in the form[52]

$$H_1^{3D} = \mu_{200} + \mu_{020} + \mu_{002},$$
$$H_2^{3D} = \mu_{200}\mu_{020} + \mu_{020}\mu_{002} + \mu_{200}\mu_{002} - \mu_{110}^2,$$
$$H_3^{3D} = \mu_{200}\mu_{020}\mu_{002} - \mu_{002}\mu_{110}^2 \quad (1)$$

where μ_{pqr} is the normalized central moment[52]

$$\mu_{pqr} = V^{-(p+q+r+3)/3} \times \int_V \mathrm{d}V(x - x_0)^p (y - y_0)^q (z - z_0)^r \quad (2)$$

and where V and (x_0, y_0, z_0) are the particle's volume and centroid, respectively.

The shape analysis algorithm is represented schematically in Figure 3. First, the 3D particle shapes are parametrized using

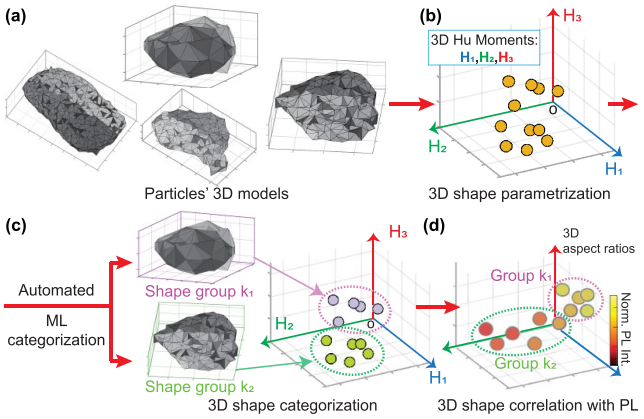

Figure 3. Representation of quasi-3D shape categorization via unsupervised machine learning. (a) Exemplar 3D particle shape models. (b) Parametrization of shapes using 3D Hu moments H_1, H_2, and H_3. (c) Shape categorization is achieved by *k*-means clustering-based machine learning applied to the Hu moments (shape groups are color coded). (d) Transformation of the 3D shape space from Hu moments to an alternative shape descriptor and correlation with PL measurements.

3D Hu moments, such that each particle can be expressed as a point in the 3D Hu space (Figure 3(b)). Second, unsupervised machine learning is used to categorize the shapes based on *k*-means clustering with the average-linkage method[53] (Figure 3(c)). The number of shape groups are optimally chosen using internal cluster validity indexes[54−56] (see SI Section VI for further details). Finally, the parametrized and categorized particle shapes are correlated with their PL measurements to exhibit 3D structure−fluorescence correlations (Figure 3(d)).

Additionally, we can further utilize the normalized central moments to compute a *visual* shape descriptor.[41] In this case, we chose the 3D aspect ratio, and the reason for this choice will become clear below. The 3D aspect ratios (η_x, η_y, η_z) can be defined in terms of the particle axes' lengths

$$\eta_x = (Y + Z)/2X,$$
$$\eta_y = (Z + X)/2Y,$$
$$\eta_z = (X + Y)/2Z \quad (3)$$

where X and Y are the major and minor horizontal axis lengths, respectively, and Z is the vertical axis length. The axis lengths themselves can be written in terms of the normalized central moments, given in the form (details of the derivation are given in SI Section V)

$$X = \sqrt{10}\,V^{1/3} \times (\mu_{200} + \mu_{020} + ((\mu_{200} + \mu_{020})^2 + 4\mu_{110}^2)^{1/2})^{1/2},$$
$$Y = \sqrt{10}\,V^{1/3} \times (\mu_{200} + \mu_{020} - ((\mu_{200} + \mu_{020})^2 + 4\mu_{110}^2)^{1/2})^{1/2},$$
$$Z = 2\sqrt{5}\,V^{1/3}(\mu_{002})^{1/2} \quad (4)$$

(Note that the expression for Z is simpler due to the assumption that the x−y plane is a mirror plane.) Thus, for example, η_z is the ratio of the particle's average width to its height. For a perfect sphere, we have $(\eta_x, \eta_y, \eta_z) = (1, 1, 1)$. In general, a larger aspect ratio implies a thinner particle in the corresponding direction.

Another relevant and simple visual shape descriptor is the sphericity, Ψ, which measures the "compactness". The 3D sphericity is directly related to the 3D Hu moments according to

$$\Psi = \frac{H_1^{3D(S)}}{H_1^{3D}} \quad (5)$$

where $H_1^{3D(S)}$ is the first Hu moment for a perfect sphere, and H_1^{3D} is that of the particle. For a particle that happens to be a perfect sphere, the sphericity Ψ reaches its maximum value of unity.

It is worth emphasizing that, while the visual shape descriptors facilitate a simpler interpretation, retaining the more general Hu moments can also be important in ensuring that the correlations established between shape and PL brightness are free from bias.

Application to FND Morphology, Structure, and Photoluminescence. *FND Optical and Structural Properties.* The FNDs studied here were nominally 100 nm in size and were produced by irradiating synthetic diamond powders with 40 keV He^+ ions followed by annealing at 800 °C to create NV centers and air surface oxidation treatments at 450 °C for 1 h, as described in more detail elsewhere.[25,33]

Figures 4(a−d) show representative BF-TEM images of the FND particles in which the irregular nature of the particle shapes can be seen. In Figure 4(e), the FND particles show little graphitic species on the surfaces, as expected due to the surface oxidation treatment performed during the synthesis (see SI for further details). Figure 4(f) shows the particle size distribution (derived from TEM data), which is broad, ranging from approximately 20 to 250 nm, with an average size of about 100 nm. The PL spectrum in Figure 4(g) shows that the FND particles contain neutral and negatively charged NV centers, evidenced by the emission peaks at 575 and 638 nm, respectively. The excited-state lifetime measurement is shown in Figure 4(h), from which we deduce an average lifetime of ≈16 ns, which is a value typical of FND particles in this size

https://doi.org/10.1021/acsnano.3c00857
ACS Nano 2023, 17, 16491−16500

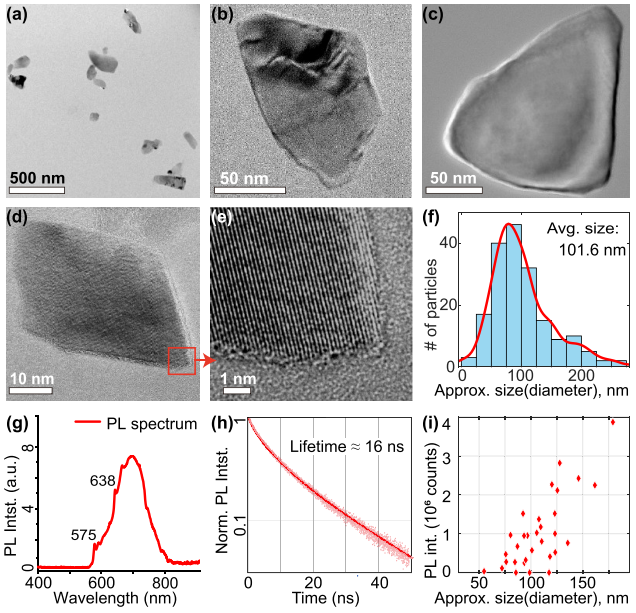

Figure 4. Structural and optical properties of FNDs. (a–d) Representative BF-TEM images showing particle size and shape distribution. (e) High-resolution BF-TEM image showing surface structure of the particle in (d). (f) Histogram of particle sizes. (g) PL spectrum. (h) Fluorescence lifetime measurement. (i) PL intensities from individual FND particles as a function of particle diameter.

range.[25] In Figure 4(i), the PL intensities obtained from individual particles (using the TEMPL method) are plotted as a function of the particle diameter. We observe an expected trend of increasing PL intensity with size, albeit with a significant scatter of up to 6-fold variation for a given particle size, in agreement with previous studies.[27,29]

FND Photoluminescence–Morphology Relationship. We applied the machine-learning-assisted correlative TEMPL method described above to analyze the fluorescence–morphology relationship of individual FND particles within the sample field of view. The PL intensities of individual particles were obtained by integrating them over an appropriate area of the background-subtracted PL map containing an isolated particle. Great care was taken to ensure that each data point refers to an isolated particle. As a result, only about 20% of the total particles were used. This precaution is necessary to overcome the relatively poor spatial resolution of the PL signal. Note, however, that the particle selection process is not based on any optical property, and so it should not introduce any bias. Of those particles that could be isolated, 98% exhibit a measurable NV fluorescence. Such a high yield for nominally 100 nm particles is in agreement with previous reports based on ensemble measurements.[26,57]

Figure 5(a) shows the categorization of the shapes of 42 selected particles in the 3D Hu space. The distribution is scattered, demonstrating the irregular nature of the FND particle shapes (compared to colloidal particles synthesized using the bottom-up approach[50,51]). Nonetheless, the automated machine learning categorization results in three relatively well-separated shape groups, k_1, k_2, and k_3. Particles in group k_1 (purple) are characterized by small Hu moments H_1, H_2, and H_3. Group k_2 (green) tends to have somewhat larger Hu moments, except H_3, which remains small. The Hu moments of group k_3 (yellow) tend to be the largest and also exhibit the most scatter. 3D particle models representative of the three groups are shown in Figure 5(j–l).

By representation of the FND shapes in 3D aspect-ratio space (Figure 5(c)) a more obvious and concentrated particle shape distribution is revealed. The distribution exhibits a specific trend, from more spherical-like shapes with (η_x, η_y, η_z) close to (1, 1, 1) to thin-flake shapes characterized by large η_z and small η_x and η_y. It is observed that all particles have $\eta_z > 1$, which is a reflection of the fact that regardless of their shape, the particles tend to reside as flatly as possible on the substrate. In terms of the shape categorization, while the three shape groups appear less distinct in aspect-ratio space, we can still broadly state that group k_1 corresponds to spherical-like particles and groups k_2 and k_3 correspond to thin flakes. The said trends are further revealed by representing the shape groups in terms of sphericity, as shown in Figure 5(h,i). It can be clearly seen that groups k_2 and k_3 have lower sphericity (<0.5) compared to group k_1.

Correlation of the PL brightness against the employed shape descriptors, namely, the 3D Hu moments H_1, H_2, and H_3, the aspect ratios η_x, η_y, and η_z, and the sphericity Ψ, is shown in Figure 5(b), (d), and (h), respectively. If the PL intensity from a given particle was simply proportional to its volume, as would reasonably be expected for a uniform distribution of identical NVs, the volume-averaged PL intensity in Figure 5(b), (d), and (h) would remain essentially constant for all particles (with fluctuations). On the contrary, Figure 5(b) shows that the majority of the particles within group k_1 have low volume-averaged PL intensities, whereas those in k_2 and k_3 have higher intensities. When representing the PL variation with respect to the aspect ratios in Figure 5(d), it can be seen that the thinner, flake-shaped particles, corresponding to groups k_2 and k_3, have significantly higher volume-averaged PL intensities (group average of 2.1 counts/nm^3) compared to the thicker, more spherical-like particles in group k_1 (group average of 0.8 counts/nm^3). Finally, Figure 5(h) exhibits a clear trend that the volume-averaged PL intensity is inversely proportional to the particle sphericity (with the exception of a few outliers).

With the assumption that the number of NVs within a particle is proportional to its volume, the results in Figure 5(b), (d), and (h) translate to the statement that individual NVs within thinner, flake-shaped particles are brighter. These results also explain at least some of the scatter observed in the PL intensities in Figure 4(i) and previous studies,[27,29] since those measurements do not account for the 3D particle shapes.

Theoretical Analysis of Purcell Effect. As mentioned in the Introduction, a wide range of phenomena have been reported to influence the NV fluorescence in FNDs. However, the phenomenon arguably most directly linked to particle shape is the Purcell effect, whereby the modes of the electromagnetic field, which are available to the photons emitted and absorbed by the NVs, are altered with respect to a homogeneous medium. To investigate this effect, we performed simulations of the relevant electric fields and their influence on the probability of detecting NV centers (see SI Section VIII). The simulations assume disc-shaped particles 100 nm in diameter with thicknesses in the range 10–100 nm, which match the observed particle sizes but with a simplified geometry. While the said geometry ignores the shape irregularities and surface roughness of the observed particles, we note that many of the particles are broadly flat shaped (77.4% of FNDs have aspect ratios $\eta_z > 1.5$; see Figure 5(c)) and that the measured surface roughness is small (typically less than 5 nm; see Figure S10).

https://doi.org/10.1021/acsnano.3c00857
ACS Nano 2023, 17, 16491–16500

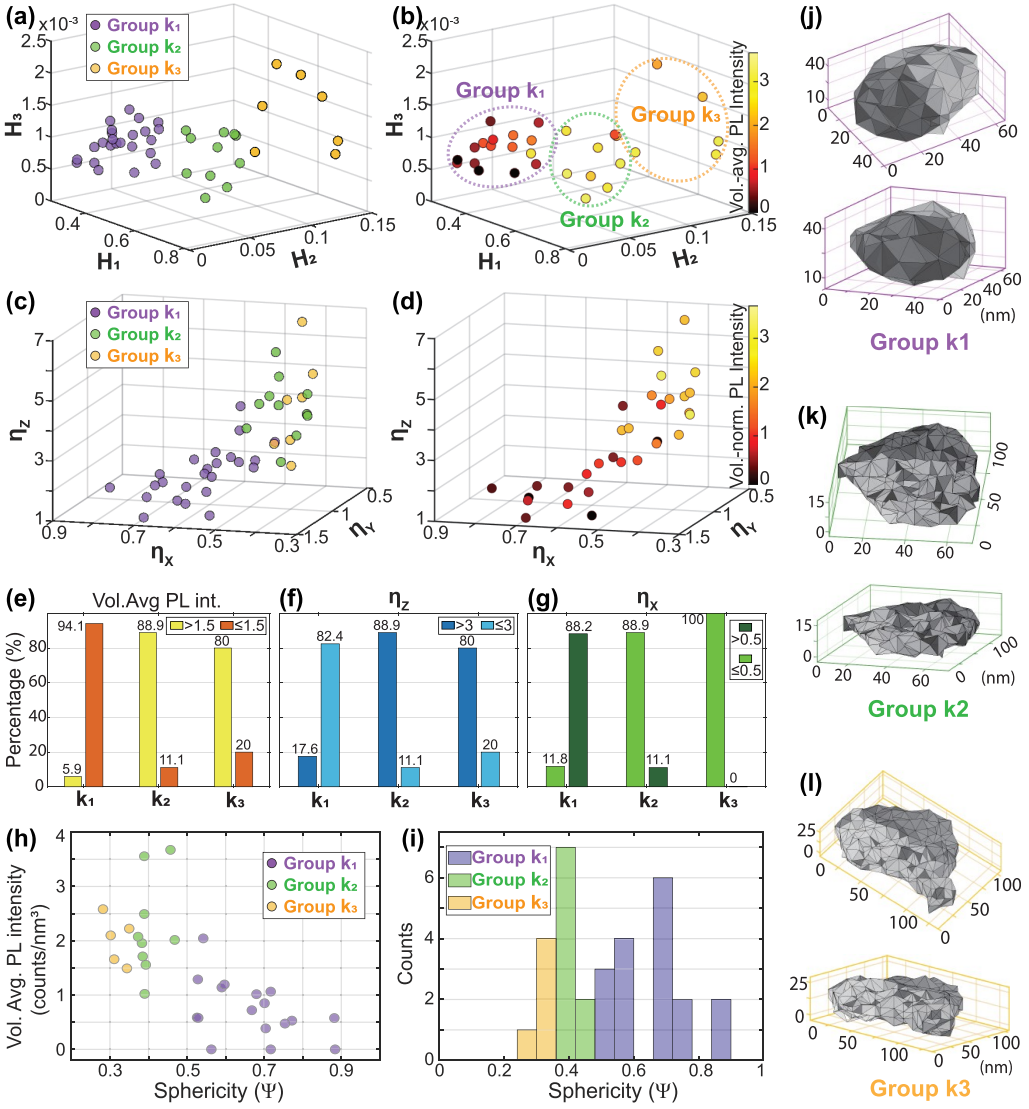

Figure 5. 3D morphology−photoluminescence relationship in FNDs. (a) Plot of individual FND particles in 3D Hu space, with shape groups k_1, k_2, and k_3 as determined by machine learning indicated. (b) Plot in 3D Hu space with color coding of points indicating volume-average PL intensity. (c) Analogous plot of (a) showing individual FND particles in 3D aspect-ratio space. (d) Plot in aspect-ratio space with color coding of points indicating volume-average PL intensity (note (b, d) contain fewer data points than (a, c) due to the spatial resolution limit of PL, as discussed in the text). (e−g) Threshold-based histograms that summarize the trends of volume-averaged PL intensities with respect to (e) Hu moment shape categorization, (f, g) 3D aspect ratios in z and x, respectively, among the shape groups k_1, k_2, and k_3. (h) Volume-averaged PL intensities of individual FND particles as a function of their sphericity Ψ. (i) Sphericity Ψ histogram of individual FND particles of the three shape groups. (j−l) 3D FND models representative of the three shape groups.

Simulations were conducted for particles supported by a 10-nm-thick Si_3N_4 substrate (matching our experiments) as well as particles in free space/air (simulating the case of particles surrounded by a medium of low refractive index). The simulations assumed a plane-wave description of the incident and detected light (for a justification of this assumption, the reader is referred to Figures S8 and S9).

Figure 6(a) shows the position-dependent probability of detecting a PL signal from an NV center within a particle, i.e., the probability of obtaining a PL signal from an NV center at a given position. The position-dependent probability is generally greater for thinner particles in both cases, and for the substrate-supported cases, this probability is significantly enhanced near the bottom side of the particle interfacing the substrate. Figure 6(b) shows the corresponding volume-averaged PL signals, where a uniform distribution of NVs has been assumed. Our simulations show that the volume-averaged PL signal is strongest for the 10-nm-thick particle and decreases with increasing particle thickness.

The prediction of greater volume-averaged PL signals in thinner, flake-shaped particles is in good agreement with our experimental observations, as shown in Figure 6(c), where a qualitative comparison between the calculation and the experimental results is given. These results indicate that the geometry of the particle *and* the substrate can have a significant influence on the PL signal from individual NVs. The results are attributable to stronger electric fields within thin, flake-shaped particles, which arise due to the constructive interference between downward propagating and upward propagating (soft reflected) partial waves in these deep-subwavelength-thick particles. With increasing particle thickness, the interference turns destructive and ultimately becomes damped due to

https://doi.org/10.1021/acsnano.3c00857
ACS Nano 2023, 17, 16491−16500

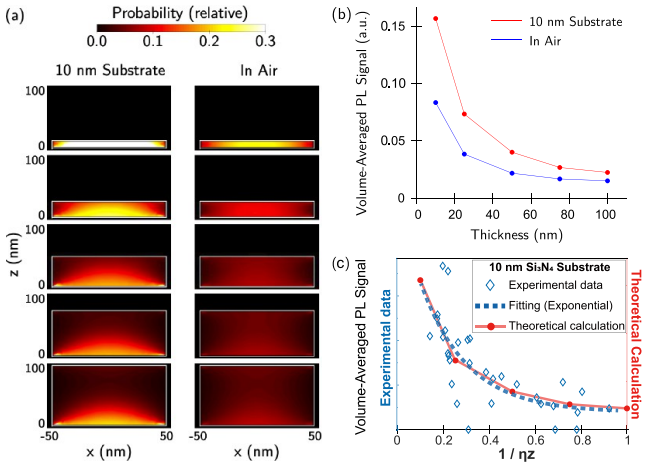

Figure 6. Purcell effect on the PL signal from diamond particles supported by a 10-nm-thick Si_3N_4 substrate (matching our experiments) and particles in air. Particles are assumed disc-shaped with a diameter of 100 nm and thicknesses of 10, 25, 50, 75, and 100 nm. (a) Position-dependent probability of detecting a PL signal from a randomly oriented NV center inside the particle, using circularly polarized 520 nm light illumination from above. (b) Volume-averaged PL signal as a function of particle thickness, assuming a uniform distribution of NVs inside the particle. (c) Qualitative comparison between the theoretical calculation (red, on the 10 nm substrate in (b)) and the experimental results (blue) with an exponential function fitting (blue dashed line).

reflections from the sides of the particles. We have no reason to suspect that the charge state of an NV center plays a significant role in this effect, and hence it should persist for both NV^0 and NV^- centers.

The greater volume-averaged PL signal from supported particles compared to those in air (and other low-index media) is ultimately due to the subwavelength thickness of the substrate: For particles in air, the reflection of partial waves from the bottom of the particle is quite strong due to the greater change in refractive index at the diamond/air interface. However, for 10 nm substrate supported particles, partial waves are reflected from both the diamond/Si_3N_4 and Si_3N_4/air interfaces, and, due to the subwavelength thickness of the substrate, these interfere constructively at locations within a few tens of nanometers of the particle's bottom surface, with a net strength ultimately greater than for a particle in air. Hence, in this picture, the subwavelength thickness of the substrate plays an important role, as it results in a high effective reflectivity, which can enhance the electric field. We note that in the presence of a *bulk* Si_3N_4 substrate, partial waves reflected from the internal diamond/Si_3N_4 interface are weaker, and so the variation of the volume-averaged PL signal with particle thickness is far less marked (Figure S6). However, as the refractive index of a bulk substrate is lowered, the enhancement grows. For particles surrounded by a medium of substantially lower refractive index, our calculations show that fluorescence enhancement persists, even for different particle orientations (see Figure S9 for calculations of the diamond disc in air). The latter remarks are particularly relevant for FNDs dispersed in solutions in biological applications.

CONCLUSIONS

In conclusion, we have introduced a machine-learning-assisted correlative TEMPL method, which enables direct elucidation of the 3D morphological−fluorescence relationship of fluorescent nanoparticles. We emphasize that the method provides three-dimensional morphological information, which is potentially crucial for a variety of fluorescent nanoparticle systems but rarely achieved. Another significant advantage is that, in contrast to ensemble-based methods, TEMPL is performed ultimately at the level of individual particles. Notwithstanding this, machine learning assistance permits the analysis of a statistically meaningful number of particles. Looking to the future, we note that there are several ways in which the TEMPL method could be extended. For example, while here we used BF-TEM imaging to provide 3D particle shape information, other TEM modalities such as ADF-STEM and EFTEM could be used. Likewise, the fluorescence measurements need not be restricted to the PL brightness but could be extended to incorporate lifetime measurements. Such extensions would significantly broaden the range of nanoparticle systems amenable to the TEMPL method.

Here we applied the TEMPL method to analyze the 3D morphology−fluorescence relationship of NV-containing nanodiamonds. The results directly reveal that the volume-averaged brightness of thin, flake-like nanodiamond particles is up to several times greater than that of three-dimensional-shaped, thicker particles provided the particle diameter is less than the subwavelength limit. With the assumption that the number of NVs within a particle is proportional to its volume, this implies that individual NVs within thinner particles are brighter. Our theoretical analysis indicates that the comparative brightness of thinner particles, either on a thin supporting substrate or in a low-index medium, is attributable, at least in part, to the constructive interference of partial light waves in these particles. With increasing particle thickness, such an effect becomes damped. The subwavelength dimension of the substrate plays an important role, as it results in higher effective reflectivity comparable to diamond particles in a low-index medium (e.g., a low-index solution). Our calculations are consistent with previous theoretical calculations,[58] which predicted similar effects. Here we emphasize the importance of the substrate thickness, as borne out by our calculations and experimental results. Our TEMPL method allows us to unambiguously demonstrate experimentally the FND shape and substrate effects on the brightness.

These results suggest potential avenues for fluorescence-optimized nanodiamonds for sensing applications. Fabrication of FNDs of controlled size and shape has recently been demonstrated using a sophisticated, top-down self-assembled mask method.[59] This method is likely better suited for quantum technologies due to the potential high cost and low production yield. Another possible route is through the core−shell particle design where the shell is composed of a thin and low-refractive-index material.[60,61] Moreover, for device applications involving particles surrounded by a low-index medium (e.g., vacuum, air, or solution) or supported by a subwavelength substrate, the greater brightness of thin, flake-shaped particles should persist for other substrate materials, or surrounding media, having a refractive index lower than the diamond.

https://doi.org/10.1021/acsnano.3c00857
ACS Nano 2023, 17, 16491−16500

METHODS/EXPERIMENTAL

Materials. The FND samples used in this study were synthesized by FND Biotech, Inc. (Taiwan). The synthesis process began with ball milling nitrogen-containing diamond powders into nanoparticles of 100 nm nominal size, followed by irradiation with 40 keV He^+ ions at a fluence of approximately 2×10^{13} cm^{-2}, followed by annealing at 800 °C for 2 h to create NV centers, as described in more detail elsewhere.[25,33] The sample was then oxidized in air at 450 °C for 1 h. The oxidation process is considered to be beneficial for two related reasons: First, it is supposed to remove non-sp^3-bonded surface species, i.e., graphitic and amorphous carbon, which are produced during the ball milling and irradiation processes,[62] as such species are considered to act as electron "traps" that result in intermittency (blinking) and quenching of the NV emission.[4] Second, oxygenated diamond surfaces can help to stabilize, or even enhance, the emission. This can be explained by the replacement of C−H surface groups that may lead to blinking of (NV^-) centers, by C−O functional groups during the surface oxidation.[21,63,64]

TEM Specimen Grid Preparation for Correlative TEMPL. After dilution with deionized water, a nanodiamond dispersion was drop-cast onto a TEM grid featuring windows of 10-nm-thick *a*-Si_3N_4 containing nine 100×100 μm^2 windows. The purpose of the dilution is to allow the nanoparticles to be distributed on the TEM grid with a suitable degree of dispersion, i.e., neither too dense or forming large clusters to interfere with the correlation of isolated FND particles nor too dispersed to have too few particles in the image. The *a*-Si_3N_4 substrate film not only avoids the unwanted fluorescence from the *a*-C that is present on more traditional TEM grids but also produces minimal background fluorescence as well as low background contrast for TEM imaging. Moreover, the thin substrate serves to closely mimic the electromagnetic environment that FND particles would experience in free space. The same TEM specimens were used in both TEM and confocal PL experiments, to achieve direct correlative electron-light microscopy.

Transmission Electron Microscopy Measurements. A JEOL F200 TEM was used to obtain a BF-TEM image stack and high-resolution TEM images. An in-house automated script was used to control the movement of the stage and image acquisition to perform sequential BF-TEM imaging over the entire region of interest. An in-house software written in MatLab was used to generate the BF-TEM image stack into a TEM montage and further to analyze the particle size and shape information. In addition, aberration-corrected TEM, GrandArm2, operated at 300 kV, was used to obtain HRTEM images as well as C K-edge electron energy loss spectroscopy.

Confocal Fluorescence Microscopy and Spectroscopy. A custom-built scanning confocal fluorescence microscope with a high numerical aperture (NA) objective lens (100× magnification, NA = 0.9) operating at room temperature was used (see diagram of the instrument setup in Section I in the SI). A tunable and pulsed (20 ps pulse width) white light laser (SuperK Extreme, NKT Photonics, Denmark) was used as a light source. Avalanche photodiodes (SPCM-AQRH-14, Excelitas Technologies, USA) were employed for imaging, and a spectrometer (Princeton Instruments, SpectraPro with a PIXIS CCD camera) to obtain fluorescence spectra. A correlator card (TimeHarp 260, Picoquant, Germany) was used to obtain time-resolved direct fluorescence decay traces. The fluorescence signal was separated from the 520 nm excitation beam using a 532 nm dichroic and long-pass optical filter (both Semrock, USA). Images were acquired using a piezo scanning stage (PInanoXYZ, PhysikInstrumente, Germany). Another in-house software written in MatLab was used to extract particle PL intensity data from PL maps.

Correlation of PL and TEM Data. To match the 3 orders of magnitude difference in the fields of view of PL and TEM, 1521 (39 × 39) individual TEM images covering the same region of interest were acquired to produce a BF-TEM montage map, which can be correlated with the PL map. Correlation of the PL and TEM image data mandated corrections to both the PL map and the TEM montage image in order to achieve an accuracy of better than 1 nm. The main corrections involved were as follows: residual skew correction of TEM images, anisotropic scaling of the PL map, image translation, and rotation to match the two images. A detailed schematic can be found in the SI. After the one-to-one TEMPL correlation is established, the corresponding single-particle size and shape information and PL intensity information are integrated.

Simulations of PL Signals in Theoretical Calculation. In the simulations, we assumed disc-shaped 100 nm diameter particles with thicknesses ranging from 10 to 100 nm, containing uniformly distributed NV centers. The diamond particles and the silicon nitride substrate were modeled as lossless dielectrics with constant refractive indices $n_d = 2.417$ and $n_s = 2.046$. The particles were surrounded by a spherical perfectly matched layer with a radius λ_0 and thickness $\lambda_0/3$, where λ_0 is the vacuum wavelength (520 nm for incident light and 638 nm for detected light, the latter corresponding to a negatively charged NV center). An extra fine mesh, calibrated for general physics, was used throughout.

Here, each NV center is approximated as a dipole that can undergo excitation by photon absorption and radiative decay by photon emission. A circularly polarized plane wave, incident from above, was sampled within the particle at points representing defects occupying equal particle volumes. At each of these points, the electron fields for the excitation (associated with the 520 nm ingoing plane wave) and detected radiative decays (associated with the 638 nm outgoing plane wave boundary condition) were calculated for the PL signal simulation. Calculations of the above electric fields were performed in the frequency domain by using the Comsol Multiphysics RF Module.

Calculations for diamond particles supported by a bulk Si_3N_4 substrate were also performed; more details of simulation and results can be found in the SI.

ASSOCIATED CONTENT

Supporting Information

The Supporting Information is available free of charge at https://pubs.acs.org/doi/10.1021/acsnano.3c00857.

Further details including a diagram of in-house confocal PL setup; correlation of PL and TEM data; validation of BF-TEM intensity−thickness relationship using ADF-STEM and AFM; construction of 3D morphology of particles; parametrization of 3D shape information; particle shape categorization; IR spectroscopy and EELS of FND; simulation of PL signals; surface roughness measurement by AFM (PDF)

AUTHOR INFORMATION

Corresponding Author

Shery L. Y. Chang − *School of Materials Science and Engineering, University of New South Wales, Sydney, NSW 2052, Australia; Electron Microscope Unit, Mark Wainwright Analytical Centre, University of New South Wales, Sydney, NSW 2052, Australia;* orcid.org/0000-0001-7514-4584; Email: shery.chang@unsw.edu.au

Authors

Haotian Wen − *School of Materials Science and Engineering, University of New South Wales, Sydney, NSW 2052, Australia*

David Kordahl − *Department of Physics and Engineering, Centenary College of Louisiana, Shreveport, Louisiana 71104, United States*

Inga C. Kuschnerus − *School of Materials Science and Engineering, University of New South Wales, Sydney, NSW 2052, Australia; Electron Microscope Unit, Mark Wainwright Analytical Centre, University of New South Wales, Sydney, NSW 2052, Australia*

Philipp Reineck − *ARC Centre of Excellence for Nanoscale Bio Photonics, School of Science, RMIT University, Melbourne, VIC 3004, Australia;* orcid.org/0000-0003-1549-937X

Alexander Macmillan − *BMIF, Mark Wainwright Analytical Centre, University of New South Wales, Sydney, NSW 2052, Australia*

Huan-Cheng Chang − *Institute of Atomic and Molecular Sciences, Academia Sinica, Taipei 10617, Taiwan;* orcid.org/0000-0002-3515-4128

Christian Dwyer − *Electron Imaging and Spectroscopy Tools, Sans Souci, NSW 2219, Australia; Physics, School of Science, RMIT University, Melbourne, Victoria 3001, Australia*

Complete contact information is available at: https://pubs.acs.org/10.1021/acsnano.3c00857

Notes

The authors declare no competing financial interest.

ACKNOWLEDGMENTS

H.W., C.D., and S.L.Y.C. acknowledge the use of TEMs (JEOL F200 and GrandArm2) at the Electron Microscope Unit, Mark Wainwright Analytical Centre, UNSW. S.L.Y.C. acknowledges the use of instruments in the Spectroscopy Facility at the University of Sydney. P.R. acknowledges support through an Australian Research Council DECRA Fellowship (grant no. DE200100279) and an RMIT University Vice-Chancellor's Research Fellowship. H.W. acknowledges support of Tuition Fee Scholarship (TFS) by UNSW Sydney. S.L.Y.C. acknowledges support by the Australian Research Council (ARC) under grants IC210100056 and DP230101847.

REFERENCES

(1) Barnard, A. S. Diamond standard in diagnostics: nanodiamond biolabels make their mark. *Analyst* **2009**, *134*, 1751−1764.

(2) Wu, Y.; Cao, S.; Alam, M. N. A.; Raabe, M.; Michel-Souzy, S.; Wang, Z.; Wagner, M.; Ermakova, A.; Cornelissen, J. J.; Weil, T. Fluorescent nanodiamonds encapsulated by Cowpea Chlorotic Mottle Virus (CCMV) proteins for intracellular 3D-trajectory analysis. *J. Mater. Chem. B* **2021**, *9*, 5621−5627.

(3) Schirhagl, R.; Chang, K.; Loretz, M.; Degen, C. L. Nitrogen-vacancy centers in diamond: nanoscale sensors for physics and biology. *Annu. Rev. Phys. Chem.* **2014**, *65*, 83−105.

(4) Bradac, C.; Gaebel, T.; Naidoo, N.; Sellars, M.; Twamley, J.; Brown, L.; Barnard, A.; Plakhotnik, T.; Zvyagin, A.; Rabeau, J. Observation and control of blinking nitrogen-vacancy centres in discrete nanodiamonds. *Nat. Nanotechnol.* **2010**, *5*, 345−349.

(5) Wu, Y.; Alam, M. N. A.; Balasubramanian, P.; Ermakova, A.; Fischer, S.; Barth, H.; Wagner, M.; Raabe, M.; Jelezko, F.; Weil, T. Nanodiamond theranostic for light-controlled intracellular heating and nanoscale temperature sensing. *Nano Lett.* **2021**, *21*, 3780−3788.

(6) Zhang, S.-C.; Li, S.; Du, B.; Dong, Y.; Zheng, Y.; Lin, H.-B.; Zhao, B.-W.; Zhu, W.; Wang, G.-Z.; Chen, X.-D.; Guo, G.-C.; Sun, F.-W. Thermal-demagnetization-enhanced hybrid fiber-based thermometer coupled with nitrogen-vacancy centers. *Optical Materials Express* **2019**, *9*, 4634−4643.

(7) Dolde, F.; Fedder, H.; Doherty, M. W.; Nöbauer, T.; Rempp, F.; Balasubramanian, G.; Wolf, T.; Reinhard, F.; Hollenberg, L. C.; Jelezko, F.; Wrachtrup, J. Electric-field sensing using single diamond spins. *Nat. Phys.* **2011**, *7*, 459−463.

(8) Tian, Y.; Nusantara, A. C.; Hamoh, T.; Mzyk, A.; Tian, X.; Perona Martinez, F.; Li, R.; Permentier, H. P.; Schirhagl, R. Functionalized fluorescent nanodiamonds for simultaneous drug delivery and quantum sensing in HeLa cells. *ACS Appl. Mater. Interfaces* **2022**, *14*, 39265−39273.

(9) Bourgeois, E.; Jarmola, A.; Siyushev, P.; Gulka, M.; Hruby, J.; Jelezko, F.; Budker, D.; Nesladek, M. Photoelectric detection of electron spin resonance of nitrogen-vacancy centres in diamond. *Nature Comm.* **2015**, *6*, 1−8.

(10) Stürner, F. M.; Brenneis, A.; Kassel, J.; Wostradowski, U.; Roelver, R.; Fuchs, T.; Nakamura, K.; Sumiya, H.; Onoda, S.; Isoya, J.; Jelezko, F. Compact integrated magnetometer based on nitrogen-vacancy centres in diamond. *Diamond Relat. Mater.* **2019**, *93*, 59−65.

(11) Grazioso, F.; Patton, B. R.; Delaney, P.; Markham, M. L.; Twitchen, D. J.; Smith, J. M. Measurement of the full stress tensor in a crystal using photoluminescence from point defects: The example of nitrogen vacancy centers in diamond. *Appl. Phys. Lett.* **2013**, *103*, 101905.

(12) Tisler, J.; Reuter, R.; Lämmle, A.; Jelezko, F.; Balasubramanian, G.; Hemmer, P. R.; Reinhard, F.; Wrachtrup, J. Highly efficient FRET from a single nitrogen-vacancy center in nanodiamonds to a single organic molecule. *ACS Nano* **2011**, *5*, 7893−7898.

(13) Miller, B. S.; Bezinge, L.; Gliddon, H. D.; Huang, D.; Dold, G.; Gray, E. R.; Heaney, J.; Dobson, P. J.; Nastouli, E.; Morton, J. J. L.; McKendry, R. A. Spin-enhanced nanodiamond biosensing for ultrasensitive diagnostics. *Nature* **2020**, *587*, 588−676.

(14) Reineck, P.; Capelli, M.; Lau, D.; Jeske, J.; Field, M.; Ohshima, T.; Greentree, A.; Gibson, B. Bright and photostable nitrogen-vacancy fluorescence from unprocessed detonation nanodiamond. *Nanoscale* **2017**, *9*, 497−502.

(15) Barnard, A. S. Optimal vacancy concentrations to maximize the N−V yield in nanodiamonds. *Materials Horizons* **2014**, *1*, 286−291.

(16) Havlik, J.; Petrakova, V.; Rehor, I.; Petrak, V.; Gulka, M.; Stursa, J.; Kucka, J.; Ralis, J.; Rendler, T.; Lee, S.-Y.; Reuter, R.; Wrachtrup, J.; Ledvina, M.; Nesladek, M.; Cigler, P. Boosting nanodiamond fluorescence: towards development of brighter probes. *Nanoscale* **2013**, *5*, 3208−3211.

(17) Terada, D.; Segawa, T. F.; Shames, A. I.; Onoda, S.; Ohshima, T.; Osawa, E.; Igarashi, R.; Shirakawa, M. Monodisperse five-nanometer-sized detonation nanodiamonds enriched in nitrogen-vacancy centers. *ACS Nano* **2019**, *13*, 6461−6468.

(18) Osswald, S.; Yushin, G.; Mochalin, V.; Kucheyev, S. O.; Gogotsi, Y. Control of sp2/sp3 carbon ratio and surface chemistry of nanodiamond powders by selective oxidation in air. *J. Am. Chem. Soc.* **2006**, *128*, 11635−11642.

(19) Petráková, V.; Taylor, A.; Kratochvílová, I.; Fendrych, F.; Vacík, J.; Kučka, J.; Štursa, J.; Cígler, P.; Ledvina, M.; Fišerová, A.; Kneppo, P.; Nesládek, M. Luminescence of nanodiamond driven by atomic functionalization: towards novel detection principles. *Adv. Funct. Mater.* **2012**, *22*, 812−819.

(20) Bray, K.; Previdi, R.; Gibson, B. C.; Shimoni, O.; Aharonovich, I. Enhanced photoluminescence from single nitrogen-vacancy defects in nanodiamonds coated with phenol-ionic complexes. *Nanoscale* **2015**, *7*, 4869−4874.

(21) Fu, K.-M.; Santori, C.; Barclay, P.; Beausoleil, R. Conversion of neutral nitrogen-vacancy centers to negatively charged nitrogen-vacancy centers through selective oxidation. *Appl. Phys. Lett.* **2010**, *96*, 121907.

(22) Kim, M.; Mamin, H.; Sherwood, M.; Rettner, C.; Frommer, J.; Rugar, D. Effect of oxygen plasma and thermal oxidation on shallow nitrogen-vacancy centers in diamond. *Appl. Phys. Lett.* **2014**, *105*, 042406.

(23) Torelli, M. D.; Nunn, N. A.; Shenderova, O. A. A perspective on fluorescent nanodiamond bioimaging. *Small* **2019**, *15*, 1902151.

(24) Shenderova, O. A.; Shames, A. I.; Nunn, N. A.; Torelli, M. D.; Vlasov, I.; Zaitsev, A. Synthesis, properties, and applications of fluorescent diamond particles. *J. Vac. Sci. Technol. B* **2019**, *37*, 030802.

(25) Su, L.-J.; Fang, C.-Y.; Chang, Y.-T.; Chen, K.-M.; Yu, Y.-C.; Hsu, J.-H.; Chang, H.-C. Creation of high density ensembles of nitrogen-vacancy centers in nitrogen-rich type Ib nanodiamonds. *Nanotechnology* **2013**, *24*, 315702.

(26) Hsiao, W. W.-W.; Hui, Y. Y.; Tsai, P.-C.; Chang, H.-C. Fluorescent Nanodiamond: AVersatile Tool for Long-Term Cell

Tracking, Super-Resolution Imaging, and Nanoscale Temperature Sensing. *Acc. Chem. Res.* **2016**, *49*, 400−407.
(27) Reineck, P.; Trindade, L. F.; Havlik, J.; Stursa, J.; Heffernan, A.; Elbourne, A.; Orth, A.; Capelli, M.; Cigler, P.; Simpson, D. A.; Gibson, B. C. Not all fluorescent nanodiamonds are created equal: a comparative study. *Particle & Particle Systems Characterization* **2019**, *36*, 1900009.
(28) Shulevitz, H. J.; Huang, T.-Y.; Xu, J.; Neuhaus, S. J.; Patel, R. N.; Choi, Y. C.; Bassett, L. C.; Kagan, C. R. Template-Assisted Self-Assembly of Fluorescent Nanodiamonds for Scalable Quantum Technologies. *ACS Nano* **2022**, *16*, 1847−1856.
(29) Mohtashami, A.; Koenderink, A. F. Suitability of nanodiamond nitrogen−vacancy centers for spontaneous emission control experiments. *New J. Phys.* **2013**, *15*, 043017.
(30) Cuche, A.; Drezet, A.; Sonnefraud, Y.; Faklaris, O.; Treussart, F.; Roch, J.-F.; Huant, S. Near-field optical microscopy with a nanodiamond-based single-photon tip. *Opt. Express* **2009**, *17*, 19969−19980.
(31) Maletinsky, P.; Hong, S.; Grinolds, M. S.; Hausmann, B.; Lukin, M. D.; Walsworth, R. L.; Loncar, M.; Yacoby, A. A robust scanning diamond sensor for nanoscale imaging with single nitrogen-vacancy centres. *Nat. Nanotechnol.* **2012**, *7*, 320−324.
(32) Eldemrdash, S.; Thalassinos, G.; Alzahrani, A.; Sun, Q.; Walsh, E.; Grant, E.; Abe, H.; Greaves, T. L.; Ohshima, T.; Cigler, P.; et al. Fluorescent HPHT nanodiamonds have disk-and rod-like shapes. *Carbon* **2023**, *206*, 268−276.
(33) Chang, Y.-R.; Lee, H.-Y.; Chen, K.; Chang, C.-C.; Tsai, D.-S.; Fu, C.-C.; Lim, T.-S.; Tzeng, Y.-K.; Fang, C.-Y.; Han, C.-C.; Chang, H.-C.; Fann, W. Mass production and dynamic imaging of fluorescent nanodiamonds. *Nat. Nanotechnol.* **2008**, *3*, 284−288.
(34) Rondin, L.; Dantelle, G.; Slablab, A.; Grosshans, F.; Treussart, F.; Bergonzo, P.; Perruchas, S.; Gacoin, T.; Chaigneau, M.; Chang, H.-C.; Jacques, V.; Roch, J.-F. Surface-induced charge state conversion of nitrogen-vacancy defects in nanodiamonds. *Phys. Rev. B* **2010**, *82*, 115449.
(35) Fu, C.-C.; Lee, H.-Y.; Chen, K.; Lim, T.-S.; Wu, H.-Y.; Lin, P.-K.; Wei, P.-K.; Tsao, P.-H.; Chang, H.-C.; Fann, W. Characterization and application of single fluorescent nanodiamonds as cellular biomarkers. *Proc. Natl. Acad. Sci. U. S. A.* **2007**, *104*, 727−732.
(36) Zhou, L.; Cai, M.; Tong, T.; Wang, H. Progress in the correlative atomic force microscopy and optical microscopy. *Sensors* **2017**, *17*, 938.
(37) Umakoshi, T.; Fukuda, S.; Iino, R.; Uchihashi, T.; Ando, T. High-speed near-field fluorescence microscopy combined with high-speed atomic force microscopy for biological studies. *Biochimica et Biophysica Acta (BBA)-General Subjects* **2020**, *1864*, 129325.
(38) Xu, X.; Saghi, Z.; Gay, R.; Möbus, G. Reconstruction of 3D morphology of polyhedral nanoparticles. *Nanotechnology* **2007**, *18*, 225501.
(39) Midgley, P. A.; Dunin-Borkowski, R. E. Electron tomography and holography in materials science. *Nat. Mater.* **2009**, *8*, 271−280.
(40) Jacob, M.; Sorel, J.; Pinhiero, R. B.; Mazen, F.; Grenier, A.; Epicier, T.; Saghi, Z. Correlative STEM-HAADF and STEM-EDX tomography for the 3D morphological and chemical analysis of semiconductor devices. *Semicond. Sci. Technol.* **2021**, *36*, 035006.
(41) Flusser, J.; Suk, T.; Zitová, B. *2D and 3D Image Analysis by Moments*; John Wiley and Sons: Chichester, UK, 2016.
(42) Ham, H.; Wesley, J.; Hendra, H. Computer Vision Based 3D Reconstruction: A Review. *International Journal of Electrical and Computer Engineering* **2019**, *9*, 2394−2402.
(43) Jia, C. L.; Mi, S. B.; Barthel, J.; Wang, D. W.; Dunin-Borkowski, R. E.; Urban, K. W.; Thust, A. Determination of the 3D shape of a nanoscale crystal with atomic resolution from a single image. *Nat. Mater.* **2014**, *13*, 1044−1049.
(44) Backer, A. D.; Jones, L.; Lobato, I.; Altantzis, T.; Goris, B.; Nellist, P. D.; Bals, S.; Aert, S. V. Three-dimensional atomic models from a single projection using Z-contrast imaging: Verification by electron tomography and opportunities. *Nanoscale* **2017**, *9*, 8791−8798.
(45) Lebeau, J.; Findlay, S.; Allen, L.; Stemmer, S. Standardless atom counting in scanning transmission electron microscopy. *Nano Lett.* **2010**, *10*, 4405−4408.
(46) Van Aert, S.; Batenburg, K. J.; Rossell, M. D.; Erni, R.; Van Tendeloo, G. Three-dimensional atomic imaging of crystalline nanoparticles. *Nature* **2011**, *470*, 374−377.
(47) Dwyer, C.; Maunders, C.; Zheng, C.; Weyland, M.; Tiemeijer, P.; Etheridge, J. Sub-0.1 nm-resolution quantitative scanning transmission electron microscopy without adjustable parameters. *Appl. Phys. Lett.* **2012**, *100*, 191915.
(48) Dwyer, C. Quantitative annular dark-field imaging in the scanning transmission electron microscope—a review. *J. Phys. Mater.* **2021**, *4*, 042006.
(49) Hu, M.-K. Visual pattern recognition by moment invariants. *IRE Transactions on Information Theory* **1962**, *8*, 179−187.
(50) Wen, H.; Luna-Romera, J. M.; Riquelme, J. C.; Dwyer, C.; Chang, S. L. Statistically representative metrology of nanoparticles via unsupervised machine learning of TEM Images. *Nanomaterials* **2021**, *11*, 2706.
(51) Wen, H.; Xu, X.; Cheong, S.; Lo, S.-C.; Chen, J.-H.; Chang, S. L.; Dwyer, C. Metrology of convex-shaped nanoparticles via soft classification machine learning of TEM images. *Nanoscale Advances* **2021**, *3*, 6956−6964.
(52) Žunić, J.; Hirota, K.; Dukić, D.; Aktaş, M. A. On a 3D analogue of the first Hu moment invariant and a family of shape ellipsoidness measures. *Machine Vision and Applications* **2016**, *27*, 129−144.
(53) Hartigan, J. A.; Wong, M. A. Algorithm AS 136: A k-means clustering algorithm. *J. R. Stat. Soc. C (Appl. Stat.)* **1979**, *28*, 100−108.
(54) Rousseeuw, P. J. Silhouettes: a graphical aid to the interpretation and validation of cluster analysis. *Journal of Computational and Applied Mathematics* **1987**, *20*, 53−65.
(55) Davies, D. L.; Bouldin, D. W. A cluster separation measure. *IEEE Transactions on Pattern Analysis and Machine Intelligence* **1979**, *PAMI-1*, 224−227.
(56) Caliński, T.; Harabasz, J. A dendrite method for cluster analysis. *Communications in Statistics-theory and Methods* **1974**, *3*, 1−27.
(57) Yu, S.-J.; Kang, M.-W.; Chang, H.-C.; Chen, K.-M.; Yu, Y.-C. Bright fluorescent nanodiamonds: no photobleaching and low cytotoxicity. *J. Am. Chem. Soc.* **2005**, *127*, 17604−17605.
(58) Plakhotnik, T.; Aman, H. NV-centers in nanodiamonds: How good they are. *Diamond Relat. Mater.* **2018**, *82*, 87−95.
(59) Zheng, J.; Lienhard, B.; Doerk, G.; Cotlet, M.; Bersin, E.; Kim, H. S.; Byun, Y.-C.; Nam, C.-Y.; Kim, J.; Black, C. T.; et al. Top-down fabrication of high-uniformity nanodiamonds by self-assembled block copolymer masks. *Sci. Rep.* **2019**, *9*, 1−6.
(60) Inam, F. A.; Grogan, M. D.; Rollings, M.; Gaebel, T.; Say, J. M.; Bradac, C.; Birks, T. A.; Wadsworth, W. J.; Castelletto, S.; Rabeau, J. R.; et al. Emission and nonradiative decay of nanodiamond NV centers in a low refractive index environment. *ACS Nano* **2013**, *7*, 3833−3843.
(61) Prabhakar, N.; Näreoja, T.; von Haartman, E.; Karaman, D. Ş; Jiang, H.; Koho, S.; Dolenko, T. A.; Hänninen, P. E.; Vlasov, D. I.; Ralchenko, V. G.; et al. Core−shell designs of photoluminescent nanodiamonds with porous silica coatings for bioimaging and drug delivery II: application. *Nanoscale* **2013**, *5*, 3713−3722.
(62) Smith, B. R.; Gruber, D.; Plakhotnik, T. The effects of surface oxidation on luminescence of nanodiamonds. *Diamond Relat. Mater.* **2010**, *19*, 314−318.
(63) Kumar, R.; Singh, D. K.; Kumar, P.; Kumar, R.; Dhakate, S. Influence of degree of air oxidation and functionality on ensemble emission from nitrogen vacancy centers in nano-diamonds. *Diamond Relat. Mater.* **2019**, *97*, 107431.
(64) Bradac, C.; Gaebel, T.; Pakes, C. I.; Say, J. M.; Zvyagin, A. V.; Rabeau, J. R. Effect of the nanodiamond host on a nitrogen-vacancy color-centre emission state. *Small* **2013**, *9*, 132−139.

https://doi.org/10.1021/acsnano.3c00857
ACS Nano 2023, 17, 16491−16500